

**1 The Signature and Elimination of Sediment
2 Reverberations on Submarine Receiver Functions**

3 Ziqi Zhang^{1*}, and Tolulope Olugboji¹

4 ¹ Department of Earth and Environmental Sciences, University of Rochester, NY

5 Corresponding author: Ziqi Zhang (ziqi.zhang@rochester.edu)

6 Key Points:

- 7 • A dereverberation filter is proposed to eliminate the sediment reverberation effects**
- 8 on receiver functions of OBS data.**
- 9 • The proposed filter is proven effective and robust to small errors in sediment**
- 10 properties using synthetic modeling.**
- 11 • A Moho of 8.6 km depth and a sharp discontinuity of the lithosphere asthenosphere**
- 12 transition of 72 km depth is observed.**

13 Abstract

14 While the receiver function technique has been successfully applied to high-resolution
15 imaging of sharp discontinuities within and across the lithosphere, it has been shown,
16 however, that it suffers from severe limitations when applied to seafloor seismic recordings.
17 This is because the water and sediment layer could strongly influence the receiver function
18 traces, making detection and interpretation of crust and mantle layering difficult. This effect
19 is often referred to as the singing phenomena in marine environments. Here, we show how
20 one can silence this singing effect. We demonstrate, using analytical and synthetic waveform
21 modeling, that this singing effect can be reversed using dereverberation filters tuned to
22 match the elastic property of each layer. We apply the filter approach to high-quality
23 earthquake records collected from the *NoMelt* seismic array deployed on normal, mature
24 (~70 Ma) Pacific seafloor. An appropriate filter designed using the elastic properties of the
25 underlying sediments, and obtained from prior studies, greatly improves the detection of Ps
26 conversions generated from the moho (~8.6 km) and from a sharp discontinuity (<~ 5 km)
27 across the lithosphere asthenosphere transition (~72 km). Sensitivity tests show that the
28 filter is robust to small errors in the sediment properties. Our analysis suggests that
29 appropriately filtering out the sediment reverberations from ocean seismic data could make
30 inferences on subsurface structure more robust. We expect that this study will enable
31 high-resolution receiver function imaging of the base of the oceanic plate across a growing
32 fleet of ocean bottom seismic arrays being deployed in the global oceans.

33 1.0 Introduction

34 The seismic structure of the normal oceanic lithosphere-asthenosphere system is pivotal to
35 our understanding of global geodynamics and plate tectonics (Kawakatsu & Utada, 2017;
36 Olugboji, Park, Karato, et al., 2016; C. Rychert et al., 2020; C. A. Rychert et al., 2018b). For
37 instance, understanding how seismic velocities are affected by temperature, melt or
38 attenuation, can shed light on how the oceanic plate evolves and what the likely causes are
39 for the rheological transition from a rigid lithosphere to a weak asthenosphere (Karato, 2012;
40 Kawakatsu et al., 2009; Ma et al., 2020; Olugboji, Park, & Karato, 2016; C. Rychert et al.,
41 2020). While multiple seismic techniques (e.g., surface waves, SS precursors, Ps and Sp
42 converted waves, etc.) are often unanimous about the presence of a high velocity lithospheric
43 lid underlain by a low velocity asthenosphere interior, these techniques have different
44 resolution and sensitivities to the sharpness of the velocity gradient (Eaton et al., 2009;
45 Olugboji et al., 2013) and, therefore, need to be used in a complementary manner.

46 The new seismic profiles derived from the higher resolution body-wave techniques differ
47 from the early studies from surface waves, in that they identify a sharp and distinct seismic
48 discontinuity across the thermal boundary layer, suggesting modifications to the simple
49 plate-cooling models (Karato & Park, 2018; Kawakatsu & Utada, 2017; C. A. Rychert et al.,
50 2018a). One scenario invokes a unique role for partial melting and anisotropy (Hirschmann,
51 2010; Kawakatsu et al., 2009; C. A. Rychert et al., 2018a), while another seeks to explain
52 these observation using a sub-solidus attenuation mechanism (Karato & Park, 2018;
53 Olugboji et al., 2013; Olugboji, Park, Karato, et al., 2016) to explain a sharp and large
54 velocity reversal that can be age dependent. A systematic receiver function study of normal
55 oceanic mantle at various seafloor ages seems to support the latter view: an observed
56 age-dependence in sharpness and depth for the oceanic mantle especially where no
57 azimuthal dependence in seismic velocities (Olugboji, Park, Karato, et al., 2016).

58 In principle, the receiver function technique should provide the best resolution on the
59 age-dependence, depth, and sharpness of a sharp velocity gradient, making it a promising
60 seismic technique for investigating the lithosphere structure of an oceanic plate (Akuhara et
61 al., 2016, 2017; Akuhara & Mochizuki, 2015; Audet, 2016; K. Hannemann et al., 2017;
62 Janiszewski & Abers, 2015; Kawakatsu et al., 2009; P. Kumar et al., 2011; Liu et al., 2020;
63 Olugboji, Park, Karato, et al., 2016; C. a. Rychert et al., 2013; C. A. Rychert et al., 2018a).
64 However, it has been pointed out that in the seafloor environment they can be complicated
65 by sediment reverberations and should be treated with caution (Audet, 2016; Kawakatsu &
66 Abe, 2016; Olugboji, Park, & Karato, 2016).

67 The challenge of interpreting the receiver functions using seafloor seismic data results from
68 near-surface reverberations obscuring weaker conversions from deeper crust and mantle
69 discontinuities, making structural inference unreliable (Audet, 2016). The scattered wavefield
70 trapped in the overlying water column and the soft sediment layer generate a loud ringing in
71 receiver function traces, a behaviour that is very pronounced for sediment layers which
72 generate resonance modes at high frequencies, e.g., along the coastal plain or in slow
73 shear-wave sediments. While techniques for removing the water reverberations have long

74 been studied in marine environments (Backus, 1959), and by applying a wavefield
75 decomposition approach (Bostock & Trehu, 2012; Osen et al., 1999; Thorwart & Dahm,
76 2005), only recently has the water-filter approach been applied to the source-deconvolved
77 receiver function traces aiding interpretation of ocean lithospheric structure (Akuhara et al.,
78 2016, 2017; Akuhara & Mochizuki, 2015). These techniques have focused on removing
79 water-column reverberations, and while the filters are easy to design, no study has yet been
80 applied to removing the sediment reverberations in the deep ocean environments, even
81 though similar techniques have been applied to suppressing sediment reverberations
82 observed on receiver functions obtained from continental seismometers (Cunningham &
83 Lekic, 2019; Yu et al., 2015).

84 In this study, we generalize the inverse-water filter approach used in (Akuhara & Mochizuki,
85 2015; Backus, 1959) to design a two-stage filter that suppresses both the water-column and
86 sediment-layer reverberations, the latter being more severe in its effect on receiver function
87 analysis (Audet, 2016; K. Hannemann et al., 2017; Katrin Hannemann et al., 2016;
88 Kawakatsu & Abe, 2016; Olugboji, Park, & Karato, 2016). By using synthetic wavefield
89 modeling, we demonstrate that an appropriate dereverberation filter for removing offending
90 reverberations can be designed by tuning to the relevant elastic properties of the sediment
91 layer, i.e., thickness and shear velocity contrast at the sediment-crust interface. The filter is
92 prescribed completely by the two-way travel times and the reflectivity of the water-sediment
93 or the sediment-crust interfaces (Aki & Richards, 2002). We describe why this approach is
94 preferred to the empirical procedure of using the autocorrelation of the receiver functions
95 used with continental seismometers (Cunningham & Lekic, 2019; Yu et al., 2015).

96 We illustrate our methodology by designing an appropriate dereverberation filter for receiver
97 functions, calculated using ocean bottom seismological (OBS) data, obtained from the
98 *NoMelt* experiment located on mature (~ 70 Ma) Pacific seafloor. We describe how the
99 receiver function results obtained after application of the filter show that the sedimentary
100 layer reverberations can be successfully attenuated and the interpretation of deeper crust or
101 lithospheric layering improved. We compare our high-frequency receiver function results
102 with previous body wave (Gaherty et al., 1996; Tan & Helmberger, 2007), attenuation (Ma et
103 al., 2020) and conductivity constraints (Sarafian et al., 2015) in the NoMelt region, and
104 discuss its implication for models of oceanic lithosphere asthenosphere structure (Karato &
105 Park, 2018; Olugboji et al., 2013; C. Rychert et al., 2020).

106 2.0 Receiver Function for Deep Seafloor Seismometers

107 Receiver functions (RFs) are aptly named because they recover receiver-side structure
108 underneath a seismic station after the source and path effects have been removed following
109 either the deconvolution of the horizontal waveform by the vertical waveform (Ps-RFs) or
110 vice-versa (Sp-RFs) (Bostock, 2004; Rondenay, 2009). In the marine environment, even after
111 the source effects have been removed, the strong influence of the sediments beneath the
112 receiver may still obscure interpretation of deeper receiver-side structure (Kawakatsu & Abe,
113 2016). In this section, we describe the behavior of each reverberation layer and how their
114 effects can be removed from the receiver function traces by a matched dereverberation filter.

115 A successful application of the dereverberation filter can be judged by how well the response
 116 of the crust and mantle layering can be recovered from the filtered RFs. We do this by using
 117 a parameter search based on correctly predicting the travel times and relative amplitudes of
 118 the appropriate scattered phases. In the deep marine environments, we show that knowledge
 119 of the elastic properties of the sediments is key to recovering crust and mantle layering.

120 2.1 Identifying and Removing Water and Sediment Resonances

121 The significance of reverberations generated in the offshore environment, from an ocean
 122 water column and sedimentary layer, have long been recognized as one of the most
 123 challenging factors that hamper investigating deeper crustal and mantle structures using
 124 ocean bottom seismometer data (Backus, 1959; Godin & Chapman, 1999; Kawakatsu &
 125 Abe, 2016). In the shallow offshore environment, the reverberation from the ocean water
 126 column traps seismic waves while they are reflected at both the sea surface and the seafloor,
 127 causing the vertical component records of the OBSs to be masked by the water
 128 reverberations (Akuhara & Mochizuki, 2015; Audet, 2016). When pressure data is available,
 129 this can be used to suppress the water layer conversions using a wavefield decomposition
 130 approach (Bostock & Trehu, 2012; Osen et al., 1999; Thorwart & Dahm, 2005). Previous
 131 studies have shown that the effects of the water column are not severe in the deep marine
 132 waters since the water reverberations arrive later in the P coda (Audet, 2016), however, they
 133 may still interfere with signals from deeper velocity discontinuities, e.g.,
 134 lithosphere-asthenosphere boundary (LAB). Additionally, a thin layer of pelagic or
 135 terrigenous sediments in such an environment could render receiver functions almost
 136 uninterpretable.

137 Our goal in this work is to suppress the negative effects of these reverberations on the
 138 receiver function traces, using a technique similar to an idea that is well-documented on
 139 land-based seismic stations (Cunningham & Lekic, 2019; Yeck et al., 2013; Yu et al., 2015).
 140 For an oceanic model with a low-velocity sedimentary layer or water column (Figure 1), the
 141 receiver function (the source-deconvolved seismograms) can be expressed as:

$$142 R(t) = \sum_{n=0}^{\infty} (-r_0)^n \tilde{R}(t - n\Delta t) \quad (1)$$

143 where R and \tilde{R} are the receiver functions with and without the influence of sedimentary
 144 layer or water column, respectively, r_0 is the reverberation strength, and Δt is the two-way
 145 travel time of the reverberated S waveleg within the sediment layer (or reverberated P
 146 waveleg within the water layer).

147 In the frequency domain, equation (1) can be expressed as (Backus, 1959; Snieder & Snieder,
 148 2001):

$$149 R(f) = \tilde{R}(f) \sum_{n=0}^{\infty} (-r_0)^n e^{-i2\pi f n \Delta t} \quad (2)$$

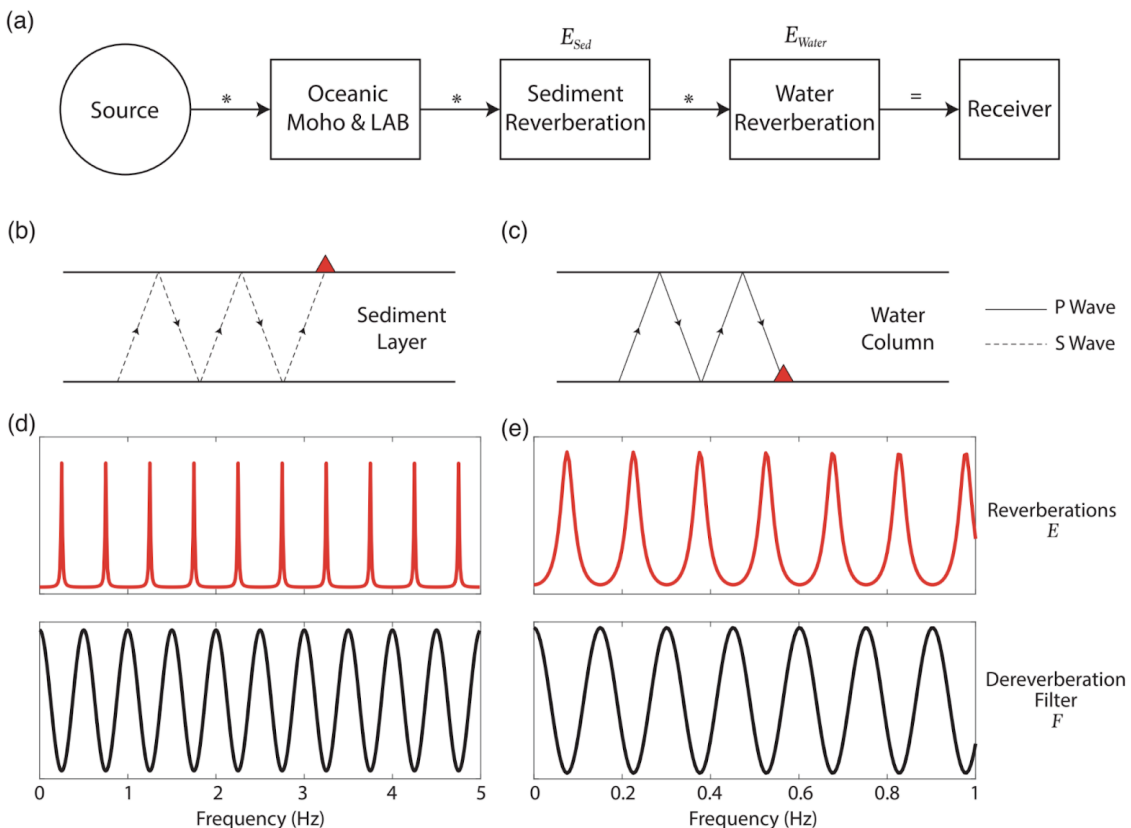
150 Notice that $\sum_{n=0}^{\infty} (-r_0)^n e^{-i2\pi f n \Delta t}$ is a geometric series that can be simplified as
 151 $(1 + r_0 e^{-i2\pi f \Delta t})^{-1}$, which allows us to write the infinite series as a linear filter in the
 152 frequency domain that causes a reverberation effect:

$$153 R(f) = \tilde{R}(f) \cdot E(f) \quad (3a)$$

$$154 \tilde{R}(f) = R(f) \cdot F(f) \quad (3b)$$

$$155 F(f) = E^{-1}(f) = (1 + r_0 e^{-i2\pi f \Delta t}) \quad (3c)$$

156 where E is the reverberation effect of the sediment or water layer, and F is the
 157 reverberation removal filter in the frequency domain, which eliminates the appropriate
 158 resonance caused by waves trapped in a water or sediment layer (notice that $E \cdot F = 1$).



159 **Figure 1.** Systematic description of the reverberations and the dereverberation filter design. (a) Wave
 160 paths of teleseismic events when sediment and water are present. (b) Sketches of S wavelegs traveling
 161 in the sediment layer causing reverberations. The red triangle denotes the station. (c) Sketches of P
 162 wavelegs traveling in the water column causing reverberations. (d) Sedimentary reverberation effects
 163 E_{Sed} (top) and the corresponding dereverberation filter F'_{Sed} (bottom) in the frequency domain.
 164 (e) Same as Figure 1d but for water reverberations E_{Water} and the corresponding filter F'_{Water} .

165 A few points can very quickly be summarized about the reverberation effect and the
 166 corresponding matched dereverberation filters. First, both the sediment and water
 167 reverberations have the same form in the frequency domain and behave as comb filters with
 168 sharp peaks at the fundamental and overtone frequencies, which are odd multiples of the

169 inverse of the two-way travel time in the respective layer. Second, to suppress the
 170 reverberation effect, the matched dereverberation filter is the appropriately scaled notch
 171 filter that removes the frequencies at which the reverberations obscure the subsurface
 172 conversions. Finally, in the global oceans, the sediment and water-column properties
 173 (velocity and thickness) vary in a predictable manner that enables us to judge their relative
 174 influence and frequency-dependence. Along the continental shelf, the water column is thin
 175 and sediments are thick, while in the deeper oceans, the case is reversed; the water column is
 176 deep and the sediments reach some terminal thickness. Since the fundamental frequency of
 177 the resonance is governed by the two-way travel in the relevant layer, it is clear that for deep
 178 oceans these frequencies are at the low-frequency end of the spectrum (Figure 1e), while the
 179 thin sediments have a higher resonance frequency (Figure 1d), which makes the removal of
 180 the sediment reverberations crucial in the deep oceans, especially if fine-scale crust and
 181 mantle layering is desired using high-frequency ($\sim 1\text{Hz}$) receiver functions (Olugboji et al.,
 182 2013).

183 In the application to land-based seismometers presented in Yu et al., (2015), the two
 184 parameters of the dereverberation filter (r_0 and Δt) can be estimated empirically from the
 185 receiver function data by finding the best-fitting decaying sinusoid to the autocorrelation
 186 function of the original receiver function in the time domain (Cunningham & Lekic, 2019):

$$187 \quad m(t) = R(t) \star R(t) \approx ce^{-at} \cos\left(\frac{\pi t}{\Delta t}\right) \quad (4)$$

188 where t is the lag time of the autocorrelated RF, Δt is the half-period of the oscillation, c is
 189 the autocorrelation amplitude at zero lag time, and a is the decay constant. Because the
 190 half-period of the oscillation is precisely the travel time of the S reverberation, $r_0 = m(\Delta t)$
 191 , the parameters of the dereverberation filter can be estimated by fitting this autocorrelation
 192 function. In our synthetic tests and marine data examples, we show that Δt and
 193 fundamental frequency, f_0 , may be used in conjunction with PbS delay time from waveform
 194 records, to jointly constrain the allowable range for the sediment velocity and thickness. In
 195 the case of sediment reverberations, once the sediment properties are known, the filter can
 196 be computed using the reflection coefficient (reverberation strength) and delay time (derived
 197 from velocity and thickness of sediments).

198 To demonstrate this, we compute synthetic receiver functions for two different oceanic plate
 199 models, M1 and M2, which highlight the different signatures of a water and sediment layer
 200 on receiver function deconvolution (Figure 2a). In this implementation, we demonstrate how
 201 the dereverberation filter is used to improve the detection of crust and upper mantle
 202 interfaces. We point out that the filter parameters can be derived from the reflection
 203 coefficients and two-way travel time for the shear (sediment) and compressional wave (water)
 204 reverberations. For ocean bottom data, the appropriate reflection coefficients is for a water
 205 layer over halfspace, where water reverberations are suppressed using an r_0 defined by the
 206 P-to-P reflection coefficient, R_{PP} , at the sea floor; whereas r_0 is the S-to-S reflection

207 coefficient, R_{SS} , for sediment reverberations (see Text S1-A in Supporting Information for
208 the analytical expressions). The two-way travel times are described by :

$$209 \quad \Delta t(p_i) = \frac{2H}{v} \sqrt{1 - v^2 p_i^2} \quad (5)$$

210 where H and v are the thickness and shear velocity of the sediment layer (or the depth and
211 P velocity of the water column), respectively; and p_i denotes the ray parameter.

212 **Table 1.** Density, velocity, and thickness parameters of various layers in the synthetic velocity
213 models.

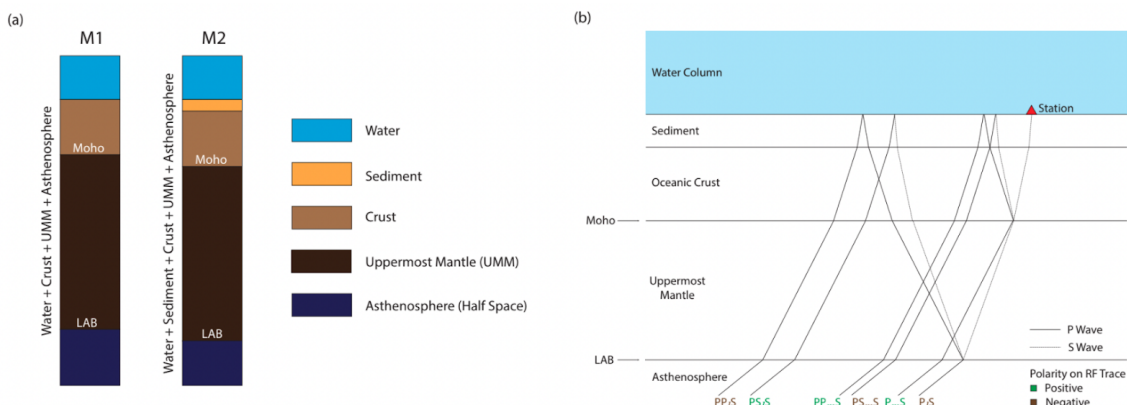
Layer	ρ (kg/m ³)	Velocity (km/s)		κ	Thickness, H (km)	
		v_p	v_s		M1	M2
Water	1027	1.50	-	-	5.0	5.0
Sediment	2000	2.00	0.50	4.00	-	0.8
Crust	2800	6.50	3.65	1.78	7.0	7.0
*UMM	3300	8.10	4.50	1.80	50.0	50.0
Asthenosphere	3200	8.10	4.10	1.98	-	-

214 *UMM = UpperMost Mantle;

215 $\rho_{w,s,c,m,hs}$: the density of water, crust, mantle, and halfspace;

216 $v_{p,s}$: P-wave and S-wave velocity respectively;

217 $\kappa = v_p/v_s$: the P to S velocity ratio.



218 **Figure 2.** Sketch of velocity models and Ps phases. (a) Representative velocity models used to
219 demonstrate RF estimation in a deep-ocean environment. Model M1 depicts an oceanic crustal and

220 upper mantle structure with no sediments. Model M2 adds a thin sedimentary layer on top of the
 221 oceanic crust in Model M1. Detailed model parameters are shown in Table 1. (b) Schematic diagrams
 222 showing the main Ps phases and their multiples from both Moho and LAB, using layered model M2
 223 described in Figure 2a. The names of the phases are labeled next to each ray path; green and brown
 224 names indicate positive and negative polarities on the RF traces, respectively.

225 2.2 Recovery of Crust & Mantle Layering: RF Interpretation

226 Successful application of a reverberation filter can be assessed by how well the receiver
 227 function traces can be interpreted for the appropriate Ps conversions and multiples. We
 228 model the phase-delay time using a grid search stacking approach to estimate the thickness
 229 (H), and P-to-S wave velocity ratio (κ), independent of the P velocity (v_p) (Bostock &
 230 Kumar, 2010; Helffrich & Thompson, 2010; M. R. Kumar & Bostock, 2008). This requires
 231 predicting the travel times of converted and reflected phases within a particular multi-layered
 232 model. For example, in a traditional grid search (Zhu & Kanamori, 2000), the travel times of
 233 the P-to-S converted phase and its reverberations for a single crustal layer at the Moho are
 234 given by:

$$235 \quad t_{P_mS} = \frac{H}{v_p} (\sqrt{\kappa^2 - p_i^2 v_p^2} - \sqrt{1 - p_i^2 v_p^2}), \quad (6a)$$

$$236 \quad t_{PP_mS} = \frac{H}{v_p} (\sqrt{\kappa^2 - p_i^2 v_p^2} + \sqrt{1 - p_i^2 v_p^2}), \quad (6b)$$

$$237 \quad t_{PS_mS} = \frac{2H}{v_p} \sqrt{\kappa^2 - p_i^2 v_p^2}. \quad (6c)$$

238 We can write this in a compact fashion using the following substitutions:

239 $A = \sqrt{\kappa^2 - p_i^2 v_p^2}$ and $B = \sqrt{1 - p_i^2 v_p^2}$. A close observation shows that the travel time
 240 ratios can be written independent of thickness H , which makes it possible to write the travel
 241 time of the multiples (t_{PP_mS} and t_{PS_mS}) in terms of the primary conversion phase t_{P_mS} :

$$242 \quad t_{PP_mS}(p_i) = \frac{A + B}{A - B} t_{P_mS}(p_i), \quad (7a)$$

$$243 \quad t_{PS_mS}(p_i) = \frac{2A}{A - B} t_{P_mS}(p_i). \quad (7b)$$

244 Since the direct conversion is typically the earliest and strongest arrival, it is easily identified
 245 in the receiver function traces; moreover, for a thin crust, it exhibits minimal moveout
 246 compared to the reference phase (zero lag RF). Therefore, we can constrain $t_{P_mS}(p_i)$ by
 247 estimating the maximum RF amplitude within an expected arrival window (e.g., around 1s
 248 for model M1). With a clear observation for $t_{P_mS}(p_i)$ estimated from the RF traces, the
 249 other parameters, κ and v_p , are obtained by stacking the RFs along the travel time
 250 trajectories for the other multiples (i.e., equation (7)). The stack is described using a 2-D grid
 251 search for $\hat{\kappa}$ and \hat{v}_p :

$$252 \quad s = \sum_i \sum_j w_j G(t_{ij}) R_j(t) \quad (8)$$

253 where s is the stacking amplitude, t_{ij} is the predicted travel time of the j th phase used (i.e.
 254 t_{PmS} , t_{PPmS} , t_{PSmS}) based on the estimated PmS arrival described in equation (7), $G(t)$
 255 is a gaussian smoothing window centered at time t , $R_j(t)$ is the j th radial receiver function
 256 trace, and w_j is the weighting factors for different phases based on the amplitudes and
 257 polarities calculated from the transmission and reflection coefficients provided in Table 2.
 258 Consequently, the optimal pair of $\hat{\kappa}$ and \hat{v}_p is obtained when the stacking amplitude, s ,
 259 reaches maximum.

260 **Table 2.** Polarities and amplitudes of Ps conversion phases and their multiples, from Moho
 261 and LAB.

Phase	M1			M2		
	Amplitude	Weight (w_i)	Polarity	Amplitude	Weight (w_i)	Polarity
PmS	0.1632	44.76%	+	0.2885	64.61%	+
$PPmS$	0.1054	28.91%	+	0.1510	33.81%	+
$PSmS$	-0.0960	-26.33%	-	-0.0070	-1.57%	-
PI/S	-0.0735	-60.29%	-	-0.1300	-72.79%	-
$PPIS$	-0.0331	-27.18%	-	-0.0475	-26.59%	-
$PSIS$	0.0153	12.53%	+	0.0011	0.63%	+

262 *The lowercase m and $/$ in the names of the phases denotes conversions at Moho and LAB. The ray
 263 paths of the phases are shown in Figure 2b. Amplitudes and weights are calculated using relevant
 264 reflection and transmission coefficients for an incoming P wave with a ray parameter of 0.08 (see
 265 Text S1-B in Supporting Information for details on calculation).

266 The first stack uses the set of travel times described in equation (7) that are independent of
 267 layer thickness, while a second stage stack proceeds by performing a 1-D line search for
 268 optimal layer thickness \hat{H} , using equation (8), with the new predicted travel times for the
 269 primary phase and multiples, after substituting κ and v_p in equation (6) with the optimal $\hat{\kappa}$
 270 and \hat{v}_p obtained from the first stack.

271 It is easy to generalize this procedure for estimating the depth of a prominent lithospheric
 272 discontinuity (LAB depth). In this case, we assume that the mantle velocities ($\hat{\kappa}_m$, \hat{v}_{pm}) are
 273 relatively well constrained, either from PREM, AK135 or a regional oceanic velocity model
 274 (Dziewonski & Anderson, 1981; Kennett et al., 1995; C. A. Rychert et al., 2018b). The stack
 275 described in equation (8) is then implemented to perform a 1-D line search for the

276 Moho-LAB thickness, where t_{ij} is now the predicted travel times of the LAB-associated
 277 phases, i.e., P/S and PP/S :

$$278 \quad t_{P_iS}(p_i) = \hat{t}'_{P_mS}(p_i) + \frac{H_{LAB}}{\hat{v}_{p_m}}(\hat{A}_m - \hat{B}_m) \quad (9a)$$

$$279 \quad t_{PP_iS}(p_i) = \hat{t}'_{P_mS}(p_i) + \frac{H_{LAB}}{\hat{v}_{p_m}}(\hat{A}_m + \hat{B}_m) \quad (9b)$$

280 where $\hat{A}_m = \sqrt{\hat{\kappa}_m^2 - p_i^2 \hat{v}_p^2}$ and $\hat{B}_m = \sqrt{1 - p_i^2 \hat{v}_p^2}$; \hat{t}'_{P_mS} is the predicted travel
 281 time of the P_mS phase calculated from equation (6a) using optimal $\hat{\kappa}$, \hat{v}_p and \hat{H} from the
 282 Moho stack.

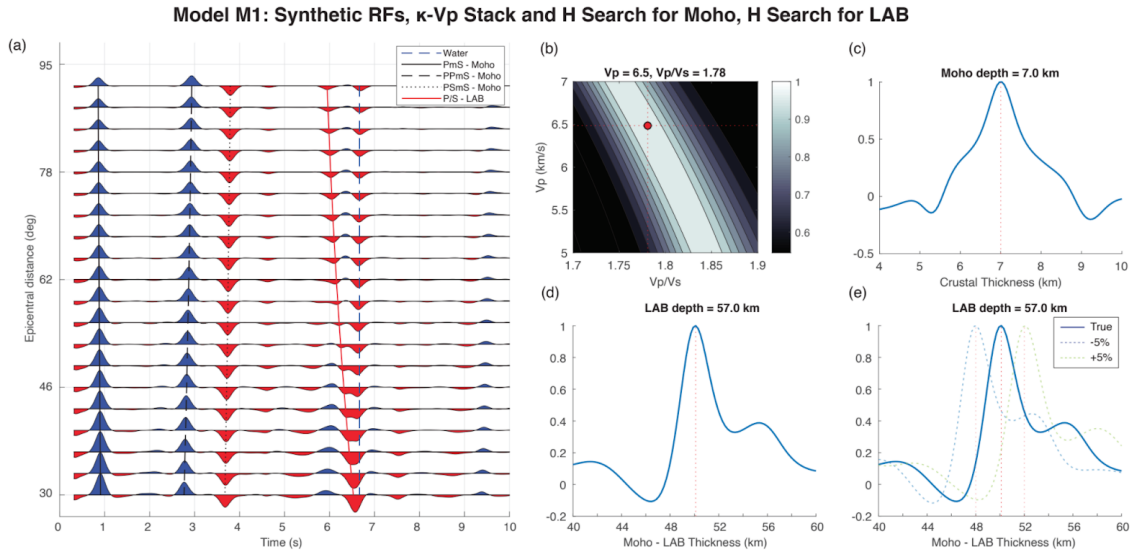
283 We note that since percent velocity change at the LAB is not as large as the Moho, the
 284 amplitudes of the reflected multiples may be insignificant. A comparison of the relative
 285 amplitude of the main P_s phases from both Moho and LAB, using velocity model M2 (Table
 286 2), shows that the relative amplitude of the second multiple from the LAB (PS_iS) is very
 287 minimal, which is why we only use the P/S and PP/S phases ($i = 1, 2$ in equation (8)). In the
 288 presence of thin sediments, these travel time equations need to be adjusted (see Text S2 in
 289 Supporting Information for the appropriate time corrections in the presence of sediments).

290 3.0 Synthetic Tests

291 We present the successful application of our dereverberation filter to receiver function traces
 292 computed using oceanic velocity models, in the presence of a water layer (M1) and both
 293 water layer and sediment layer (M2). The receiver functions are generated using reflectivity
 294 techniques and when the correct dereverberation filter is applied, the faithful recovery of
 295 crust and lithospheric layering is drastically improved.

296 3.1 Deep Ocean Model - No sediments (M1)

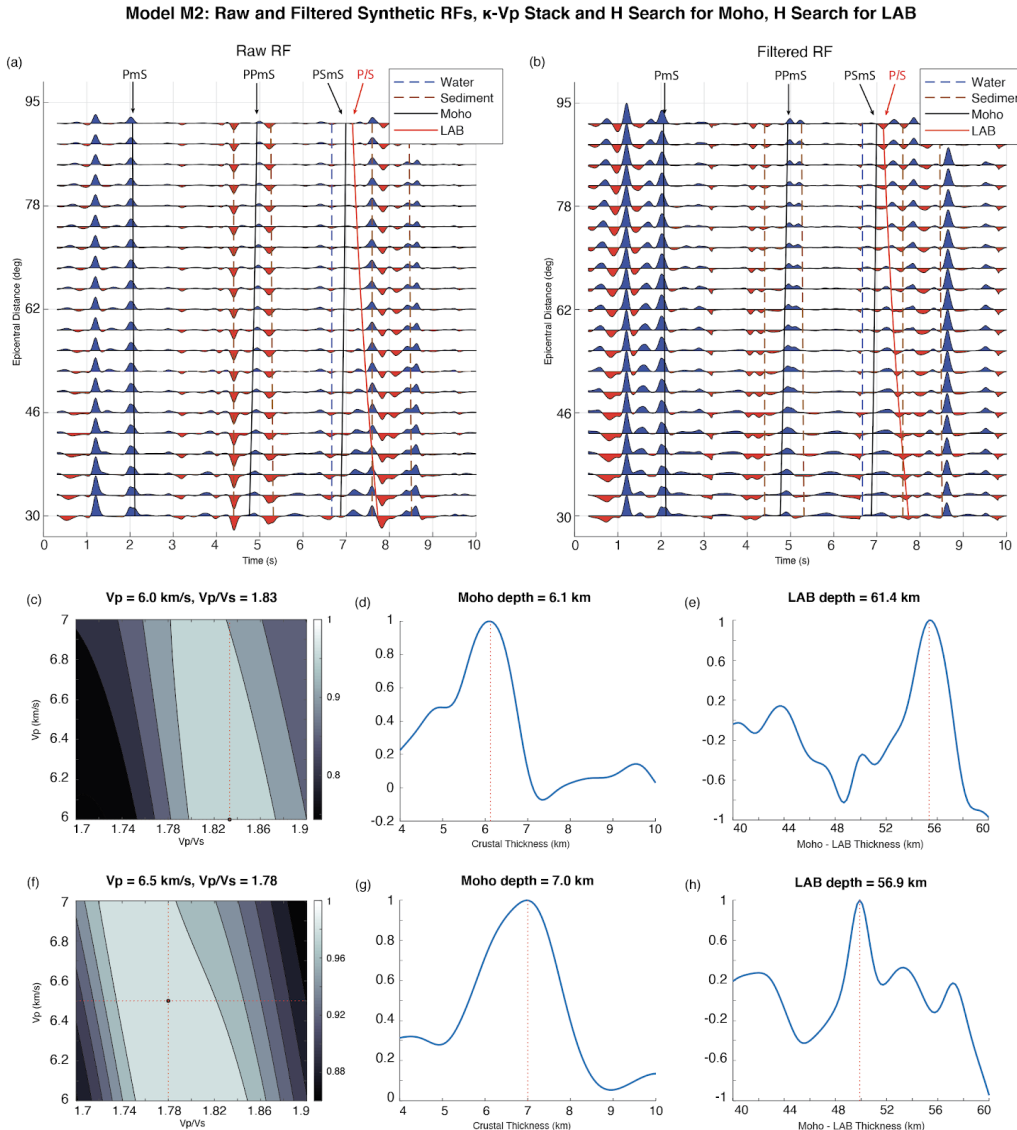
297 We compute synthetic receiver function traces at teleseismic distances for the oceanic model
 298 without sediments (M1). All major phases representing conversions and multiples from the
 299 Moho, the seismic LAB, and a first water arrival, can be clearly identified and predicted using
 300 the travel time equations (Figure 3a). The oceanic crustal P velocity and P-to-S velocity ratio
 301 are accurately predicted using the 2-D ($\kappa - v_p$) grid search (Figure 3b). Crustal thickness is
 302 also recovered by the 1-D line search (Figure 3c). The predicted values for κ , v_p , H_m are
 303 1.78, 6.5 km/s and 7.0 km, respectively, which are identical to the input model parameters
 304 for M1 (see Table 1). The 1-D line search correctly predicts the depth of the 57 km - deep
 305 seismic LAB (Figure 3d) in the presence of a closely overlapping water multiple (see Figure
 306 3a). In the LAB recovery test, we fix the mantle P velocity (8.1 km/s) and P-to-S velocity
 307 ratio (1.80) and show that the stack can recover the input values. We then show that slight
 308 errors in the mantle v_p or κ result in only a slight error in the predicted depth. For example,
 309 a 5% error in v_p (~ 0.4 km/s) would result in an error of about 3% (~ 2 km) in the seismic
 310 LAB depth (Figure 3e). This bias is within the uncertainties in our measurements.



311 **Figure 3.** Synthetic receiver function traces and parameter search showing recovery of oceanic
 312 velocity model M1. (a) RF traces plotted against epicentral distance. The predicted arrival times for
 313 direct Ps conversions and multiples from the Moho are marked as black solid, dashed and dotted
 314 lines, respectively; Ps conversion from the LAB is marked as red solid line; the first water
 315 reverberation is marked as blue dashed line. (b) $\kappa - v_p$ stack for Moho. (c) Linear search for the
 316 depth of Moho. (d) Linear search for the Moho-LAB thickness given the true κ and v_p from the
 317 velocity model (see Table 1). (e) Sensitivity of H_{LAB} to uncertainties in mantle velocities. The blue
 318 solid line is the same as in Figure 3d; blue and green dashed lines indicate linear search for the
 319 Moho-LAB thickness given positive (+5%) and negative (-5%) changes in v_p (relative to the true
 320 value defined in Table 1) with fixed true κ .

321 3.2 Deep Ocean Model in the Presence of Sediment (M2)

322 In the presence of a sedimentary layer (M2), the unfiltered synthetic receiver function traces
 323 display many more phases, the strongest being the pair of reverberations within the sediment
 324 layer (~4 - 5s and 8 - 9s). For comparison, we show the predicted timing of the Ps
 325 conversion from the Moho, LAB, water and sediment reverberations (Figure 4a). These RF
 326 traces are calculated at a high cutoff frequency of 4 Hz, to better identify the phases and
 327 demonstrate the effectiveness of the dereverberation filter. Unlike M1, the first positive peak
 328 at ~1.2 s is the Ps conversion from the bottom of sediment (PbS), while the second positive
 329 peak at ~2 s is the direct conversion from the Moho (PmS), both of which are clearly
 330 identified and separated. The first moho multiple is only slightly detectable in the RF traces
 331 at ~4.8 s ($PPmS$), since the nearby sediment reverberations are dominant. This creates a
 332 difficult situation with any stack for crustal velocity or thickness. The second moho multiple
 333 ($PSmS$) is even more difficult to detect and is barely identifiable due to its low amplitude (see
 334 Table 2). Like the direct moho phase, the conversion from the seismic LAB (P/S) is also
 335 masked by the second set of sediment reverberations (~8 s) and is hardly detectable. Figure
 336 4c-e shows the preliminary stack using these unfiltered traces. Compared to the true values,
 337 the predicted crustal P velocity (6.0 km/s), P-to-S velocity ratio (1.83), thickness (6.1 km),
 338 and LAB depth (61.4 km) have an error of about 8% (see Table 1).



339 **Figure 4.** Synthetic receiver function traces and parameter search showing recovery of oceanic
 340 velocity model M2. (a) Raw RF traces plotted against epicentral distance. The predicted arrival times
 341 for direct Ps conversions and multiples from the Moho are marked as black solid, dashed and dotted
 342 lines, respectively; Ps conversion from the LAB is marked as red solid line; the reverberations from
 343 the bottom of sediment are marked as brown dashed lines; the first water reverberation is marked as
 344 blue dashed line. (b) Filtered RF traces plotted against epicentral distance. The predicted travel times
 345 for different phases are marked the same as Figure 4a. (c) $\kappa - V_p$ stack for Moho, using raw RF
 346 shown in Figure 4a. (d) Linear search for the depth of Moho, using raw RF shown in Figure 4a. (e)
 347 Linear search for the Moho-LAB thickness given the true κ and V_p from the velocity model (see
 348 Table 1), using raw RF shown in Figure 4a. (f) $\kappa - V_p$ stack for Moho, using filtered RF shown in
 349 Figure 4b. (g) Linear search for the depth of Moho, using filtered RF shown in Figure 4b. (h) Linear
 350 search for the Moho-LAB thickness given the true κ and V_p from the velocity model (see Table 1),
 351 using filtered RF shown in Figure 4b.

352 After the synthetic receiver function traces are filtered using the two-stage dereverberation
353 filters (Figure 4b), the reverberations are suppressed and the identification of the moho
354 multiple and LAB conversions are improved. The first and strongest moho multiple, $PPmS$,
355 which was previously masked by the sediment reverberations, is now visible (~ 4.8 s). The
356 reverberations have been effectively removed, which guarantees that the Moho stack will be
357 reliable. There is also a significant improvement in the seismic LAB conversion (compare P/S
358 in Figure 4a and 4b), since with sediment reverberations effectively removed, the P/S phase
359 can be clearly identified with the correctly predicted positive travel time moveout. We show
360 substantially improved results after applying the appropriate filter, using the $\kappa - v_p$ stack
361 and H search for Moho, and H search for LAB, respectively (compare Figure 4f-h and 4c-e).
362 With clearly identifiable phases, the stacking results are much more reliable and accurate. The
363 resulting crustal P velocity (6.5 km/s), P-to-S velocity ratio (1.78), thickness (7.0 km), and
364 LAB depth (56.9 km) are nearly identical to the input velocity model (compare errors from
365 unfiltered to filtered).

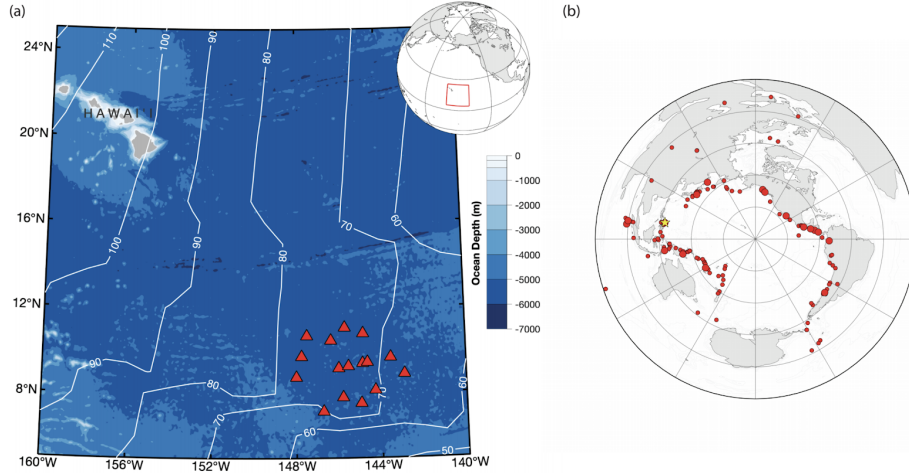
366 4.0 Real Data Examples: NoMelt Experiment

367 We use data recorded by the NoMelt experiment, which was deployed on a mature (~ 70 Ma)
368 Pacific sea floor, southeast of Hawaii, between the Clarion and Clipperton fracture zones
369 (Figure 5a), from December 2011 to December 2012. The experiment consisted of
370 broadband OBS deployment (Lin et al., 2016; Ma et al., 2020; Russell et al., 2019), an active
371 source experiment (Mark et al., 2019), and a magnetotelluric survey (Sarafian et al., 2015). We
372 process the broadband OBS data and use teleseismic events with magnitudes larger than
373 Mw6.0, located 20 to 150 degrees away from the center of the seismic array (Figure 5b).
374 Within the one-year deployment period, over 120 such earthquakes were recorded by each of
375 the 16 stations.

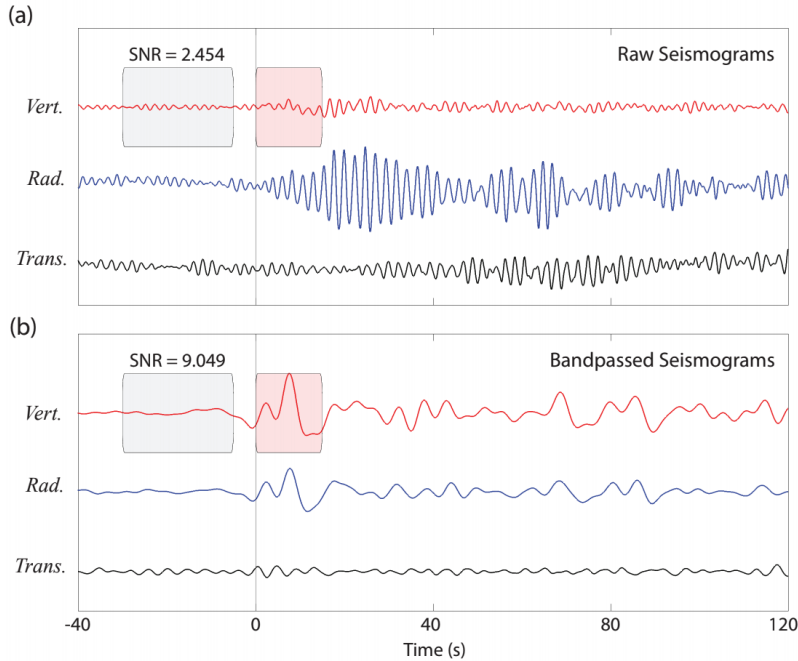
376 Ocean Bottom Seismometers are deployed remotely and without intervention, which means,
377 unlike seismometers on land, their actual horizontal orientation on the seafloor is unknown.
378 We used the reported azimuth angle from previous Rayleigh wave analysis (Adrian K. Doran
379 & Laske, 2017; Russell et al., 2019) to rotate the original seismograms to the correct ZRT
380 directions (see Figure 6).

381 To ensure robust receiver function calculations, we select the earthquake records by applying
382 an SNR (Signal-to-Noise Ratio) based quality check (QC) procedure (Figure 6). This QC
383 procedure measures the SNR of the bandpassed waveforms, and selects the events with SNR
384 > 2.0 on the vertical channel. We observe that the signal quality of the vertical seismograms
385 is degraded because of the sediment resonance which is sometimes visible as a beating
386 phenomenon (Figure 6a), caused by constructive interference of trapped modes within the
387 sediment layer (Booth et al., 2014). We therefore set the higher corner frequency of our
388 passband between 0.5 Hz and 1.0 Hz to maximize the SNR on each record and reduce the
389 effect of the sediment reverberations. The low corner frequency of the passband is set to 0.1
390 Hz to filter out the long-period tilt and compliance noise (Crawford & Webb, 2000). After
391 this QC procedure, 688 out of 2,002 records are identified for further receiver function
392 analysis, with around 40 events at each station (Table 2). The signal to noise quality of the
393 events can be seen in the average power spectra of all the events that pass quality check at

394 the NoMelt stations used in this study (Figure 7a). A comprehensive description of the signal
 395 to noise at each station indicates that some stations have better signal to noise quality on
 396 average. We refer the reader to Figure S1 in Supporting information for the complete power
 397 spectra at each NoMelt station.



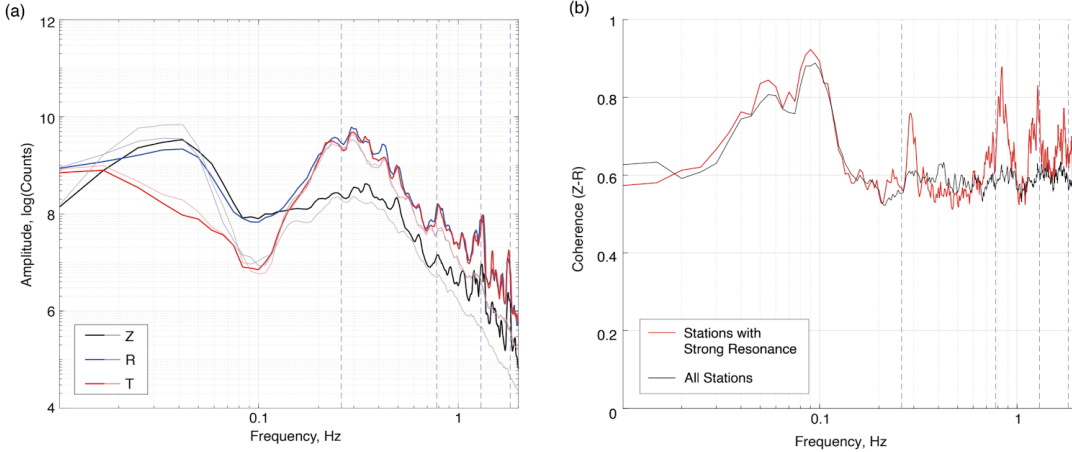
398 **Figure 5.** (a) Distribution of the OBS stations used in this study. The red triangles indicate the
 399 location of the stations. Detailed information (coordinates, elevation) can be found in Table 2. The
 400 color scale shows ocean depth; the white contour lines show the oceanic plate age in Ma (million
 401 years). The inset plot at the top right corner shows the location of the study area relative to the globe.
 402 (b) Azimuthal equidistant plot of all events used for RF analysis. Red circles indicate the location of
 403 the events; larger circles indicate events with magnitude larger than Mw7.0. The M7.6 event located
 404 at the eastern coast of the Philippines is marked as yellow pentagram, as its seismograms will be
 405 shown in Figure 6.



406 **Figure 6.** Seismograms of an M7.6 event recorded at station B13 showing the QC procedure. (a) raw
 407 seismograms; (b) bandpassed seismograms, both in Z-R-T coordinates. In the SNR calculation, signal
 408 and noise are defined as 0 - 15 s after and 20 - 5 s before the P arrival, respectively. The location of
 409 this event is marked in Figure 5a.

410 4.1 Earthquake & Noise Spectra: Signature of Sediment Resonance

411 We demonstrate the presence of sediment resonance on the NoMelt array by computing the
 412 multi-taper spectral estimates of the earthquake signals and pre-event noise. We observe
 413 sharp peaks on the earthquake signals that are absent on the noise spectra (Figure 7a). These
 414 peaks are also strongly coherent on the vertical and horizontal components at some stations,
 415 suggesting that they are signal-generated (Figure 7b). The amplitude and regularity of these
 416 peaks are strongest on the horizontal seismograms, confirming that they are
 417 sediment-induced resonances (Figure 1). The fundamental frequency is $\sim 0.3\text{Hz}$ with the
 418 peaks becoming more pronounced at high frequencies ($> 1\text{Hz}$). While the average spectra
 419 across the network can be used to estimate the sediment properties, we point out that the
 420 individual resonance at each station is more complicated, with some stations showing
 421 stronger resonance than others, and the fundamental frequency of the sediment resonance
 422 varying from station to station (see Figure S1). This is the case for sediment properties that
 423 vary slightly across the network (i.e., thickness or shear velocity). Regardless, we use an
 424 average shear velocity and thickness of the sediment to design the dereverberation filter
 425 which approximates the average sediment structure across the array.



426 **Figure 7.** (a) Mean power spectra for all events at all stations used throughout the network. Black,
 427 blue and red lines indicate vertical, radial and transverse components, respectively; solid colors and
 428 lighter colors indicate P wave signal and pre-event noise, respectively. The spectra of P wave signal
 429 was calculated for a 120 s long time window starting 20 s before the P wave arrival; the spectra of
 430 pre-event noise was calculated for a 120 s long time window starting 180 s before the P wave arrival.
 431 Blue dashed vertical lines are sedimentary reverberation frequencies calculated from equation (14)
 432 based on a 250 m - thick sediment with shear velocity of 250 m/s. Detailed power spectra for each
 433 station can be found in Figure S1 in Supporting Information. (b) Mean coherence of vertical (Z) and
 434 radial (R) components for all events used at all stations (black line) and selected stations with strong
 435 resonance: B04, B08, B17 and B26 (red line). Blue dashed lines indicate the predicted sediment
 436 reverberations, same as in Figure 7a. Detailed coherence for each station can be found in Figure S2 in
 437 Supporting information.

438 4.2 Multi-Taper Receiver Function for Noisy Ocean Data

439 Although different types of deconvolution techniques have been advocated (Bostock, 2004;
 440 Rondenay, 2009), in this study, we choose to follow the approach of multi-taper spectral
 441 coherence technique (MTC-RFs) developed by (Park & Levin, 2000, 2016), which has shown
 442 promise for high-resolution imaging of crust and mantle structure in noisy environments like
 443 ocean islands (Leahy & Park, 2005; Olugboji & Park, 2015; Park & Rye, 2019) and the
 444 seafloor ocean bottom stations (Leahy et al., 2010; Olugboji, Park, Karato, et al., 2016).

445 The multi-taper spectral coherence approach improves frequency-dependent deconvolution
 446 in the following ways: (1) using tapers that are optimized for resistance to spectral leakage
 447 and, (2) discarding the incoherent portions of the wavefield by incorporating
 448 frequency-dependent variance-weighting for stacking receiver functions from multiple
 449 events. Frequency-domain MTC receiver functions are estimated using pre-event noise and
 450 the P-SV-SH tapered seismic records, $Y_{P,SV,SH}^k$, using k eigenspectra estimates:

$$451 \quad R_{SV,SH}(f) = \frac{\sum_{k=0}^{K-1} Y_P^k(f) * Y_{SV,SH}^k(f)}{\sum_{k=0}^{K-1} Y_P^k(f) * Y_P^k(f) + S_o(f)} \quad (10)$$

452 In real data, the pre-event noise spectrum, $S_o(f)$, and frequency-dependent variance,
 453 $\sigma_i^2(f)$ for each i seismic event is used to create a weighted average receiver function:

$$454 \quad \bar{R}(f) = \frac{\sum_i^n w_i R_i(f)}{\sum_i^n w_i} \quad (11)$$

455 the weighting function, $w_i = 1/\sigma_i^2(f)$, is computed using the coherence-derived variance:

$$456 \quad \sigma_i^2 = \frac{1 - C_{P-SV}^2(f)}{(K - 1)C_{P-SV}^2(f)} |R_i(f)|^2 \quad (12)$$

457 and $C_{P-SV}^2(f)$ is the multi-taper coherence between P and SV records. For near-unity
 458 coherence, it is easy to see that the uncertainty is low (small variance) and for low coherence,
 459 the uncertainty is high (high variance). The last step in ensuring that the processed receiver
 460 functions are free from reverberations is the application of our dereverberation filter
 461 (equation (3)) in the frequency domain:

$$462 \quad \tilde{\bar{R}}(f) = \bar{R}(f) \cdot F(f) = \bar{R}(f)(1 + r_0 e^{-i2\pi f \Delta t}) \quad (13)$$

463 We will discuss, in the following section, how to determine the filter parameters, r_0 and Δt ,
 464 from the assumed velocity structures in the NoMelt region.

465 4.3 Application of a Dereverberation Filter to the NoMelt Data

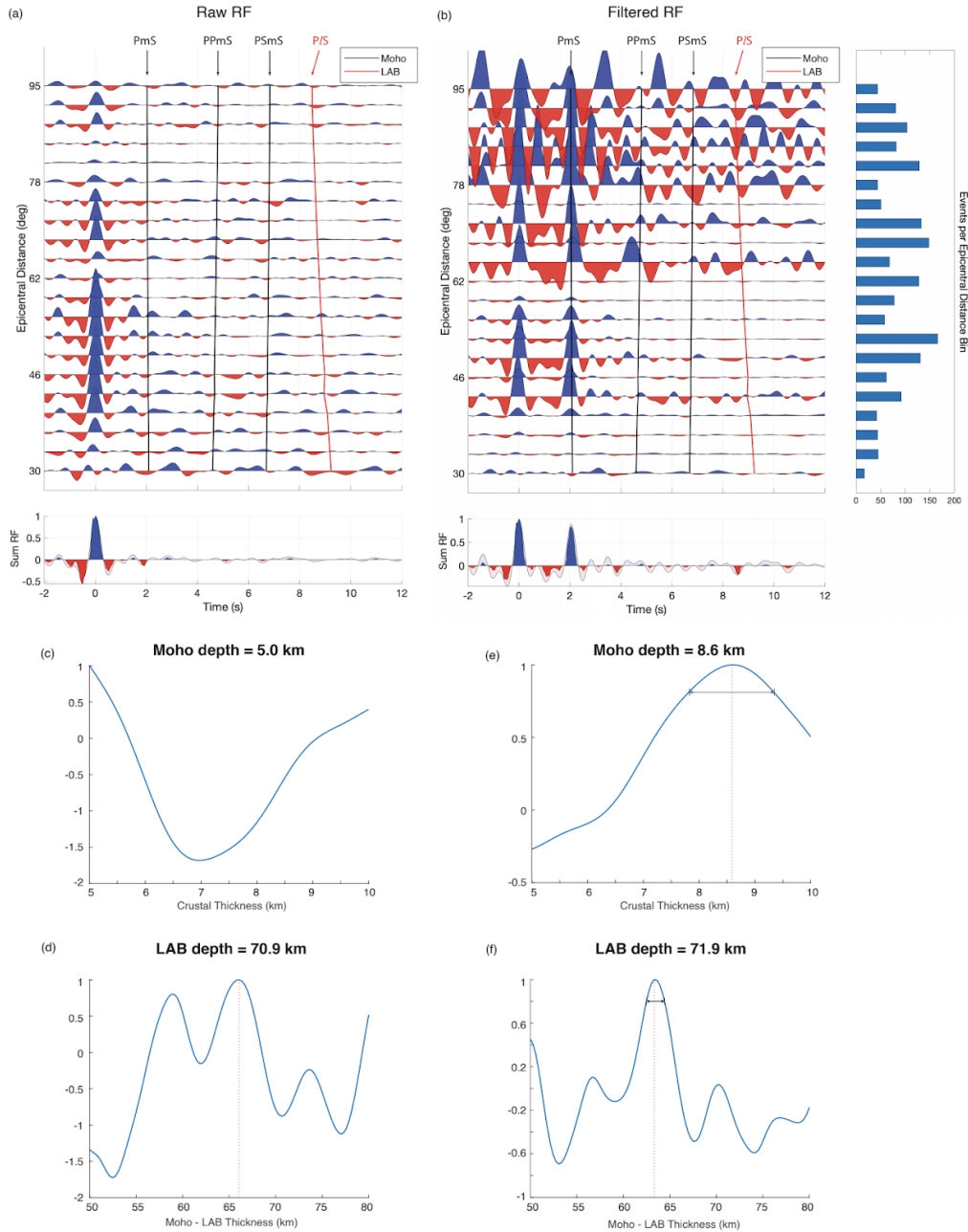
466 We use the sediment properties of 250 m thickness inferred from the refraction model and a
 467 shear velocity of 250 m/s (Ruan et al., 2014; Russell et al., 2019). The value of sediment
 468 thickness fits well with global models on sediment structure (Straume et al., 2019). The P
 469 velocity of the water column is set to 1500 m/s; the P and S velocities of the crust is set to
 470 6.5 km/s and 3.5 km/s, respectively; the P and S velocity of the uppermost mantle is set to
 471 8.1 km/s and 4.5 km/s, respectively, according to previous studies (Lin et al., 2016; Mark et
 472 al., 2019; Russell et al., 2019; Tan & Helmberger, 2007). Similar to water reverberations, the
 473 sedimentary resonant frequencies can be calculated analytically:

$$474 \quad f_n = \frac{(2n - 1)v_s}{4H_s} \quad (14)$$

475 where H_s and v_s are sediment thickness and shear velocity, respectively (Backus, 1959). We
476 compare the resonant frequencies determined using the sediment properties with the power
477 spectra obtained with multitaper spectral analysis (Figure 7a). The calculated resonant
478 frequencies match the peaks on the signal power spectra, indicating that the sediment
479 properties we choose can correctly describe the real reverberation effects. With these
480 pre-assumed sediment and crustal structures, the filter parameters, $\Delta t = 2.0$ s and $r_0 =$
481 0.90, are then specified (see equation (5) and Text S1-A in Supporting Information).

482 We calculate the receiver functions with a cutoff frequency of 1.5 Hz for all 16 stations, using
483 the multi-taper spectral coherence approach described above. We then stack all the receiver
484 function traces across the network to get a better coverage of epicentral distances (Figure
485 8a). The first P arrival is clear in raw RFs, but all Moho and LAB conversions, and their
486 multiples, are hardly visible due to severe reverberations. We apply the proposed
487 dereverberation filter to get filtered RFs (Figure 8b). After filtering, the first Ps conversion
488 from the Moho (PmS) is clearly visible at ~ 2 s; the first Moho multiple ($PPmS$), though not
489 as clear as PmS phase, is also visible at ~ 4.5 s; $PSmS$ phase is still not visible, which is
490 expected due to its low amplitude (Table 2). The first Ps conversion from the seismic LAB is
491 very clear at ~ 9 s, with the expected positive moveout, especially at higher epicentral
492 distances, which is promising in determining the LAB depth. We then implement the 1-D
493 search for Moho and seismic LAB depth to the raw and filtered RFs, given fixed ocean
494 mantle velocity structures from previous studies (Mark et al., 2019; Russell et al., 2019; Tan
495 & Helberger, 2007) (Table 1).

496 Since there are no clear positive peaks at the predicted PmS arrival time in the raw RF traces,
497 the H search for Moho using raw RFs fails, with a wrongly identified crustal thickness of 5.0
498 km, which is at the boundary of the search interval (Figure 8c). A search for the seismic LAB
499 gives a depth of 71 km; however, due to ambiguous peaks around the predicted P/S phase in
500 the RF traces, the line-search shows multiple peaks (e.g., at ~ 59 km and ~ 66 km in
501 Moho-LAB thickness in Figure 8d), making it difficult to interpret. The results using filtered
502 RF traces gives more reliable results. Using appropriate weighting for different phases (Table
503 2), we recover a crustal thickness of 8.6 ± 0.6 km (Figure 8e). Since the P/S phase is clearly
504 visible with correct moveout after applying the dereverberation filter, the results for the
505 seismic LAB shows an unambiguous major peak at the Moho-LAB thickness of 64 km,
506 giving an LAB depth of 72 ± 1 km (Figure 8f).



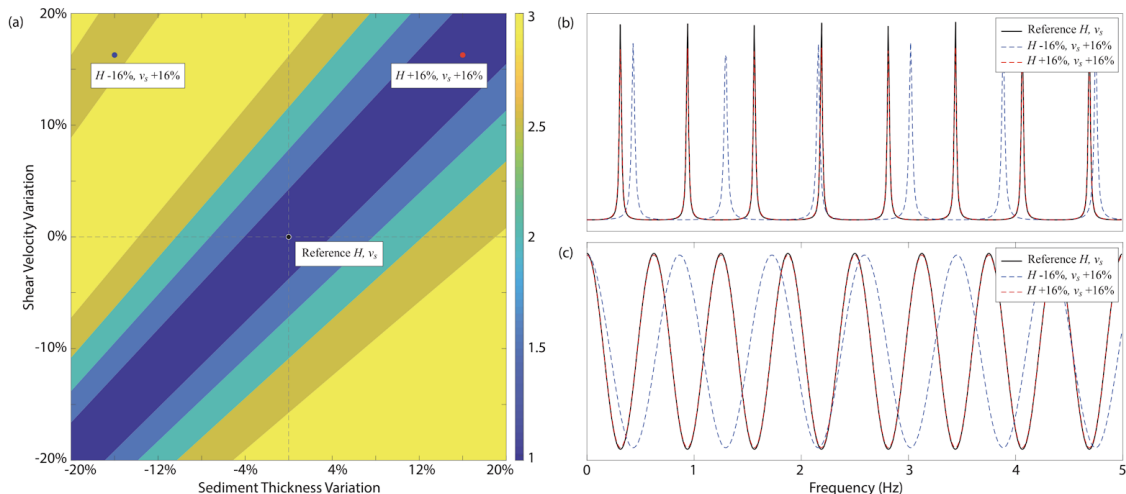
507 **Figure 8.** Receiver function traces and linear search for Moho and LAB depth using OBS data from
 508 NoMelt experiment. (a) Raw RF traces plotted against epicentral distance. The predicted arrival times
 509 for direct Ps conversions and multiples from the Moho are marked as green solid, dashed and dotted
 510 lines, respectively; Ps conversion from the LAB is marked as black solid line. (b) Filtered RF traces
 511 plotted against epicentral distance. The predicted travel times for different phases are marked the
 512 same as Figure 8a. Number of events used in each epicentral distance bin is shown in the histogram
 513 on the right. (c) Linear search for the depth of Moho given fixed crustal κ and v_p , using raw RF
 514 shown in Figure 8a. (d) Linear search for the Moho - LAB thickness given fixed crustal and mantle κ
 515 and v_p , using raw RF shown in Figure 8a. (e) Linear search for the depth of Moho given fixed crustal
 516 κ and v_p , using filtered RF shown in Figure 8b. (f) Linear search for the Moho - LAB thickness
 517 given fixed crustal and mantle κ and v_p , using filtered RF shown in Figure 8b.

518 4.4 Filter Sensitivity & Robustness

519 We note that the filter is mostly sensitive to the two-way travel time and only weakly sensitive
 520 to the reverberation strength. We show how the uncertainties in the knowledge of the
 521 sediment properties may affect the effectiveness of a slightly inaccurate dereverberation
 522 filter. For a range of sediment thicknesses and shear velocities with an unknown sediment
 523 reverberation effect, an approximate filter will still perform reliably well. The effectiveness of
 524 such a filter is quantified by a ‘robustness’ factor that describes how well it matches the
 525 reverberation effect of a sediment layer:

$$526 \quad \gamma = \left| \int_0^{1.5Hz} E(H_i, v_j, f) \right| \cdot \left| \int_0^{1.5Hz} F(H_{ref}, v_{ref}, f) \right| \quad (15)$$

527 where $E(H_i, v_j, f)$ is the reverberation effect in the frequency domain, generated using
 528 sediment thickness H_i and shear velocity v_j ; $F(H_{ref}, v_{ref}, f)$ is the filter in the
 529 frequency domain generated using the reference sediment properties ($H_{ref} = 250$ m and
 530 $v_{ref} = 250$ m/s). The mismatch between the filter and reverberations are evaluated to 1.5
 531 Hz, which is the nominal cutoff frequency at which our NoMelt receiver functions are
 532 calculated. Note that $\gamma = 1$ if $H_i = H_{ref}$ and $v_j = v_{ref}$, which is the case when the filter
 533 and the sediment properties are properly matched (equation (3c)).



534 **Figure 9.** Robustness of the dereverberation filter depending on the sediment properties. (a) The
 535 horizontal and vertical axes indicate variations in sediment thickness and shear velocity, respectively,
 536 both ranging from -20% to +20% compared to the reference sediment thickness and shear velocity:
 537 250 m and 250 m/s. The color from blue to yellow refers to the robustness factor ranging from 1 to
 538 3, indicating that the effectiveness of the reference filter on the specific sediment is lesser than that
 539 on the reference sediment. The black dot is the reference sediment thickness and shear velocity; the
 540 blue and red dots are two pairs of sediment properties. The resonance and filter generated from these
 541 sediments are shown in Figure 9b and Figure 9c. (b) Resonance of the sediment in the frequency
 542 domain. Black line: reference sediment; blue dashed line: -16% in thickness and +16% in shear

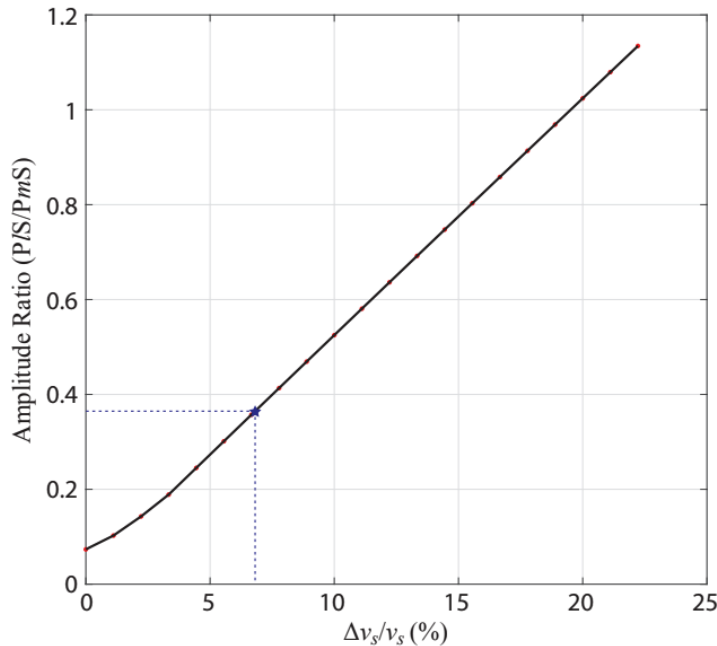
543 velocity compare to the reference sediment (blue dot in Figure 9a); red dashed line: +16% in
 544 thickness and +16% in shear velocity compare to the reference sediment (red dot in Figure 9a). (c)
 545 Corresponding filters of the resonances shown in Figure 9b.

546 The reference filter remains effective if the delay time of the filter matches that of the
 547 sediment, and can happen when the thickness and shear velocity both increase or decrease
 548 by roughly the same amount (along the bottom left - top right diagonal in Figure 9a). For
 549 example, if the sediment thickness and shear velocity both increase by 16%, the
 550 reverberations and the corresponding filters are highly alike; however, a 16% decrease in
 551 thickness and 16% increase in shear velocity could result in significant degradation of the
 552 effectiveness of the reference filter (Figure 9b-c). This indicates that the filter is mostly
 553 sensitive to the two-way travel time (equation (5)), which is proportional to the ratio of
 554 sediment thickness and shear velocity. This property means that only the ratio needs be
 555 constrained during filter design, and as we have demonstrated, may be verified using data
 556 spectra (Figure 7 and equation (14)).

557 5.0 A Sharp Velocity Reduction: ‘Seismic’ LAB of a Normal Ocean

558 The strength and sharpness of the LAB, in terms of both velocity and depth gradient, can be
 559 inferred from the width and amplitude of the pulse associated with the P_s conversion from
 560 the LAB (i.e. P/S phase) in the receiver functions. P/S phase is clearly observed at higher
 561 epicentral distance bins after applying the dereverberation filter (Figure 9b); the average
 562 width of the negative pulse of P/S phase is ~ 0.5 s. For receiver functions calculated at 1.5
 563 Hz, a 0.5 s pulse width implies a relatively sharp transition in depth of no more than 5 km
 564 (Olugboji et al., 2013).

565 The percent velocity drop at the LAB can be predicted from the relative amplitude ratio of
 566 the PmS and P/S phases in the RF traces. We generate synthetic receiver functions using
 567 different shear velocity drops at the LAB interface (while keeping other velocities fixed), and
 568 calculate the amplitude ratios between P/S and PmS phases at higher epicentral distances.
 569 The $P/S/PmS$ amplitude ratio depends on the velocity contrast across the LAB, following a
 570 roughly linear trend. A stronger velocity contrast leads to a larger amplitude for the P_s
 571 conversion from the LAB (Figure 10). We place constraints on the $P/S/PmS$ amplitude ratio,
 572 (0.37 ± 0.13), based on the PmS and P/S phases clearly visible at ~ 2 s and 9 s on the RF
 573 traces (Figure 9b). We then infer the amplitude ratio $\Delta v_s/v_s$ from our synthetic modeling,
 574 suggesting a shear velocity reduction of $\sim 6.8 \pm 2.6$ % at the LAB in the *NoMelt* region.

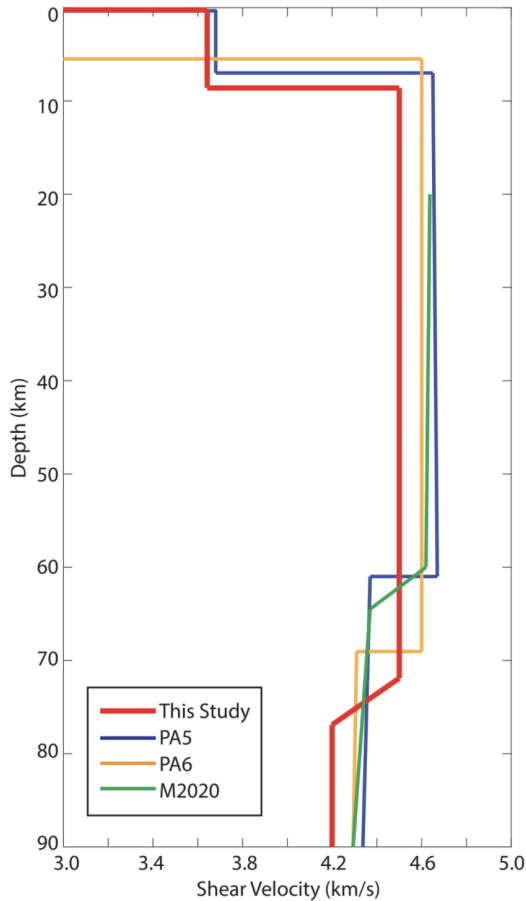


575 **Figure 10.** Determination of strength of velocity drop at the LAB from synthetic receiver functions.
 576 $\Delta v_s/v_s$ on the horizontal axis is the percentage of shear velocity drop from lithosphere to
 577 asthenosphere at the LAB. The vertical axis is the average amplitude ratio of P/S and PmS phases
 578 calculated at higher epicentral distances. The blue star indicates the predicted LAB velocity gradient
 579 at the NoMelt region from the measured amplitude ratio from filtered RF traces.

580 6.0 Discussion

581 Complementary magnetotelluric studies across the NoMelt array have shown that the
 582 lithosphere is resistive to a depth of ~ 80 km (Sarafian et al., 2015), and the transition to a
 583 conductive asthenosphere can be explained exclusively by dehydration during ocean crust
 584 formation. Surface wave attenuation measurements across the array show a transition from a
 585 low to high attenuation layer at ~ 70 km, which coincides with a transition to a low velocity
 586 layer (Ma et al., 2020). A joint assessment of the conductivity and attenuation, together with
 587 our new results on the depth (72 km) and gradient sharpness (< 5 km) of the seismic LAB
 588 structure, agrees closely with the predictions of the elastically accommodated grain-boundary
 589 sliding (EAGBS) model presented by (Karato & Park, 2018; Olugboji et al., 2013). This is
 590 broadly consistent with earlier receiver function tests from older (145 Ma) Pacific lithosphere
 591 (Olugboji, Park, Karato, et al., 2016). Our new receiver function results are broadly
 592 consistent with results from the mid-atlantic oceanic lithosphere of similar age (K.
 593 Hannemann et al., 2017), although we note that none of the past RF studies address the
 594 issue of removing sediment reverberations from ocean bottom seismic data. In the Pacific, a
 595 comparison with other body-wave techniques not affected by reverberations (e.g., SS
 596 precursors), indicates that our inferred seismic LAB depth is broadly consistent with early
 597 results (Gaherty et al., 1996; Ma et al., 2020; Tan & Helmberger, 2007) (see summary in

598 Figure 11). Although the SS precursor technique seems to show an age dependence for
 599 normal Pacific lithosphere (C. Rychert et al., 2020; C. A. Rychert et al., 2018b), the very high
 600 resolution of our receiver function results (~ 1.5 Hz) allows us to improve on the resolution
 601 of the inferred depth and sharpness of the seismic LAB.



602 **Figure 11.** Comparison of shear velocity profiles obtained in this study and some other models: PA5
 603 (Gaherty et al., 1996), PA6 (Tan & Helmberger, 2007), and M2020 (Ma et al., 2020).

604 Our approach of filtering out the sediment reverberations makes inference on subsurface
 605 structure more robust. Other proposed techniques, e.g., using band-limited receiver
 606 functions (K. Hannemann et al., 2017), or a transfer-function approach that does away with
 607 deconvolution (Akuhara et al., 2019; Audet, 2016; Thomas Bodin et al., 2014; Frederiksen &
 608 Delaney, 2015) may either be inadequate for high resolution imaging or may retain
 609 complexities that complicate the interpretation of subsurface structures, in the case of a
 610 highly reverberatory sediment layer. A band-limited receiver function approach attenuates
 611 sharp-discontinuities and masks thinly layered structures, while a transfer function approach
 612 requires a-priori constraints on the elastic properties of the sediment layer. In both cases, if
 613 the wavelength of the trapped waves in the sediment layer is similar to that of the subsurface
 614 structure it will strongly imprint on the green's function and may result in difficulty of
 615 recovering a clear image of subsurface structure (e.g., crust and mantle layering). We

616 therefore recommend an approach of tuned dereverberation filtering whenever possible,
617 especially when the signature of a sediment or shallow water reverberation is strongly
618 observed in the data spectra (e.g., Figure 7a). Even when sediment properties are not
619 completely prescribed, an appropriate filter can still be designed from empirical estimates of
620 the two-way travel time, which can be validated from the spectra or coherence
621 measurements.

622 7.0 Conclusions

623 We show that, with an appropriate filter, stable high-resolution receiver function imaging of
624 the lithosphere can be obtained from sea-floor stations and can therefore be used to
625 complement long-wavelength surface wave studies for testing models of oceanic plate origin
626 and evolution (T. Bodin et al., 2012; Gao & Lekić, 2018). We used multi-taper spectral
627 analysis to improve the detection of earthquake signals buried in noisy data and to validate
628 the parameters of our filter. We confirm that the expected resonance frequencies for the
629 sedimentary layer matches the spectra and coherence pattern of seismic data. The application
630 of a dereverberation filter to the receiver functions will be useful for a growing fleet of ocean
631 bottom deployments (Kawakatsu & Utada, 2017; C. A. Rychert et al., 2018b; Takeo et al.,
632 2018) and can advance our understanding of the origin and nature of the seismic lithosphere
633 asthenosphere boundary in the oceanic plates. In application to newly collected marine
634 seismic data (Barchek et al., 2020; Kohler et al., 2020), we anticipate that post-processing
635 the receiver functions using the recommended dereverberation filter will improve scattered
636 wave imaging, especially with amphibious seismic arrays where the water and sediment layer
637 is expected to vary significantly (Barchek et al., 2020; A. K. Doran & Laske, 2019;
638 Janiszewski & Abers, 2015; Lynner et al., 2020).

639 8.0 Acknowledgments

640 This work was made possible by grants and support from the National Science Foundation
641 under grant number: 1818654. The authors acknowledge the use of the BlueHive Linux
642 cluster at the University of Rochester's center for integrated research computing - CIRC
643 (<https://www.circ.rochester.edu/>). All seismic data used in this study can be obtained from
644 the IRIS Data management center (<https://ds.iris.edu/ds>) under network code ZA.
645 Horizontal orientations for individual stations are reported in (Russell et al., 2019) and
646 estimated using the DLOPy (Adrian K. Doran & Laske, 2017) code available on github.
647 Multi-taper spectral analysis was conducted using the MATLAB jlab library provided by
648 (Lilly, 2017). Synthetic receiver functions were computed using the telewaveism open-source
649 python library provided by (Audet et al., 2019). Reflection and transmission coefficients for a
650 two-layer model was simulated using the MATLAB code of Charles Ammon. The Receiver
651 function deconvolution was computed using compiled C++ code provided by (Olugboji &
652 Park, 2016). The binary source, Earthquake metadata, and processed receiver function SAC
653 traces can be retrieved from (Zhang & Olugboji, 2020). We acknowledge many helpful
654 discussions with Baowei Liu, Jeffrey Park, and Shun-ichiro Karato.

655 9.0 References Cited

- 656 Aki, K., & Richards, P. G. (2002). *Quantitative Seismology, 2nd Ed.*
- 657 Akuhara, T., & Mochizuki, K. (2015). Hydrous state of the subducting Philippine Sea plate inferred from receiver function image using
658 onshore and offshore data. *Journal of Geophysical Research, [Solid Earth]*, 120(12), 8461–8477.
- 659 Akuhara, T., Mochizuki, K., Kawakatsu, H., & Takeuchi, N. (2016). Non-linear waveform analysis for water-layer response and its
660 application to high-frequency receiver function analysis using OBS array. *Geophysical Journal International*, 206(3), 1914–1920.
- 661 Akuhara, T., Mochizuki, K., Kawakatsu, H., & Takeuchi, N. (2017). A fluid-rich layer along the Nankai trough megathrust fault off the Kii
662 Peninsula inferred from receiver function inversion. *Journal of Geophysical Research, [Solid Earth]*, 122(8), 6524–6537.
- 663 Akuhara, T., Bostock, M. G., Plourde, A. P., & Shinohara, M. (2019). Beyond Receiver Functions: Green's Function Estimation by
664 Transdimensional Inversion and Its Application to OBS Data. *Journal of Geophysical Research, [Solid Earth]*, 124(2), 1944–1961.
- 665 Audet, P. (2016). Receiver functions using OBS data: promises and limitations from numerical modelling and examples from the Cascadia
666 Initiative. *Geophysical Journal International*, 205(3), 1740–1755.
- 667 Audet, P., Thomson, C. J., Bostock, M. G., & Eulenfeld, T. (2019). Telewavesim: Python software for teleseismic body wave modeling.
668 *Journal of Open Source Software*, 4(44), 1818.
- 669 Backus, M. M. (1959). WATER REVERBERATIONS—THEIR NATURE AND ELIMINATION. *Geophysics*, 24(2), 233–261.
- 670 Barchek, G., Abers, G. A., Adams, A. N., Bécel, A., Collins, J., Gaherty, J. B., et al. (2020). The Alaska Amphibious Community Seismic
671 Experiment. *Seismological Research Letters*, 91(6), 3054–3063.
- 672 Bodin, T., Sambridge, M., Tkalcic, H., Arroucau, P., Gallagher, K., & Rawlinson, N. (2012). Transdimensional inversion of receiver
673 functions and surface wave dispersion. *Journal of Geophysical Research, [Solid Earth]*, 117(B2). <https://doi.org/10.1029/2011JB008560>
- 674 Bodin, T., Yuan, H., & Romanowicz, B. (2014). Inversion of receiver functions without deconvolution—application to the Indian craton.
675 *Geophysical Journal International*, 196(2), 1025–1033.
- 676 Booth, C. M., Forsyth, D. W., & Weeraratne, D. S. (2014). Upper mantle Q structure beneath old seafloor in the western Pacific. *Journal of
677 Geophysical Research, [Solid Earth]*, 119(4), 3448–3461.
- 678 Bostock, M. G. (2004). Theory and Observations -Teleseismic Body-Wave Scattering and Receiver-Side Structure. *Treatise in Geophysics*,
679 235–246.
- 680 Bostock, M. G., & Kumar, M. R. (2010). Bias in seismic estimates of crustal properties. *Geophysical Journal International*. Retrieved from
681 <https://academic.oup.com/gji/article-abstract/182/1/403/563322>
- 682 Bostock, M. G., & Trehu, A. M. (2012). Wave-field decomposition of ocean bottom seismograms. *Bulletin of the Seismological Society of America*,
683 102(4), 1681–1692.
- 684 Crawford, W. C., & Webb, S. C. (2000). Identifying and removing tilt noise from low-frequency (< 0.1 Hz) seafloor vertical seismic data.
685 *Bulletin of the Seismological Society of America*, 90(4), 952–963.
- 686 Cunningham, E., & Lekic, V. (2019). Constraining crustal structure in the presence of sediment: a multiple converted wave approach.
687 *Geophysical Journal International*, 219(1), 313–327.
- 688 Doran, A. K., & Laske, G. (2017). Ocean-Bottom Seismometer Instrument Orientations via Automated Rayleigh-Wave Arrival-Angle
689 MeasurementsOcean-Bottom Seismometer Instrument Orientations via Automated Rayleigh-Wave Arrival-Angle Measurements.
690 *Bulletin of the Seismological Society of America*, 107(2), 691–708.
- 691 Doran, A. K., & Laske, G. (2019). Seismic Structure of Marine Sediments and Upper Oceanic Crust Surrounding Hawaii. *Journal of
692 Geophysical Research, [Solid Earth]*, 124(2), 2038–2056.
- 693 Dziewonski, A. M., & Anderson, D. L. (1981). Preliminary reference Earth model. *Physics of the Earth and Planetary Interiors*, 25(4), 297–356.
- 694 Eaton, D. W., Darbyshire, F., Evans, R. L., Grüter, H., Jones, A. G., & Yuan, X. (2009). The elusive lithosphere–asthenosphere boundary
695 (LAB) beneath cratons. *Lithos*, 109(1-2), 1–22.
- 696 Frederiksen, A. W., & Delaney, C. (2015). Deriving crustal properties from the P Coda without deconvolution: the southwestern Superior
697 Province, North America. *Geophysical Journal International*, 201(3), 1491–1506.
- 698 Gaherty, J. B., Jordan, T. H., & Gee, L. S. (1996). Seismic structure of the upper mantle in a central Pacific corridor. *Journal of Geophysical
699 Research*, 101(B10), 22291.
- 700 Gao, C., & Lekic, V. (2018). Consequences of parametrization choices in surface wave inversion: insights from transdimensional Bayesian
701 methods. *Geophysical Journal International*, 215(2), 1037–1063.
- 702 Godin, O. A., & Chapman, D. M. F. (1999). Shear-speed gradients and ocean seismo-acoustic noise resonances. *The Journal of the Acoustical
703 Society of America*, 106(5), 2367.
- 704 Hannemann, K., Krüger, F., Dahm, T., & Lange, D. (2016). Oceanic lithospheric S-wave velocities from the analysis of P-wave polarization
705 at the ocean floor. *Geophysical Journal International*, 207(3), 1796–1817.
- 706 Hannemann, K., Krüger, F., & Dahm, T. (2017). Structure of the oceanic lithosphere and upper mantle north of the Gloria fault in the
707 eastern mid-Atlantic by receiver function analysis. *Journal of Geophysical Research*. Retrieved from
708 <https://agupubs.onlinelibrary.wiley.com/doi/abs/10.1002/2016JB013582>
- 709 Helffrich, G., & Thompson, D. (2010). A stacking approach to estimate VP/VS from receiver functions: Stacking to estimate VP/VS.
710 *Geophysical Journal International*, 182(2), 899–902.
- 711 Hirschmann, M. M. (2010). Partial melt in the oceanic low velocity zone. *Physics of the Earth and Planetary Interiors*, 179(1-2), 60–71.
- 712 Janiszewski, H. A., & Abers, G. A. (2015). Imaging the Plate Interface in the Cascadia Seismogenic Zone: New Constraints from Offshore
713 Receiver Functions. *Seismological Research Letters*, 86(5), 1261–1269.
- 714 Karato, S.-I. (2012). On the origin of the asthenosphere. *Earth and Planetary Science Letters*, 321-322, 95–103.
- 715 Karato, S.-I., & Park, J. (2018). On the Origin of the Upper Mantle Seismic Discontinuities. *Lithospheric Discontinuities*, 5–34.
- 716 Kawakatsu, H., & Abe, Y. (2016). Significance of sediment reverberations on receiver functions of broadband OBS data: Comments on

- 717 Olugboji et al. (2016) "Nature of the Seismic Lithosphere–Asthenosphere Boundary within Normal Oceanic Mantle from
 718 High-Resolution Receiver Functions." *Geochemistry, Geophysics, Geosystems*. <https://doi.org/10.1002/2016GC006418>
- 719 Kawakatsu, H., & Utada, H. (2017). Seismic and Electrical Signatures of the Lithosphere – Asthenosphere System of the Normal Oceanic.
 720 <https://doi.org/10.1146/annurev-earth-063016-020319>
- 721 Kawakatsu, H., Kumar, P., Takei, Y., Shinohara, M., Kanazawa, T., Araki, E., & Suyehiro, K. (2009). Seismic evidence for sharp
 722 lithosphere–asthenosphere boundaries of oceanic plates. *Science*, 324(5926), 499–502.
- 723 Kennett, B. L. N., Engdahl, E. R., & Buland, R. (1995). Constraints on seismic velocities in the Earth from traveltimes. *Geophysical Journal
 724 International*, 122(1), 108–124.
- 725 Kohler, M. D., Hafner, K., Park, J., Irving, J. C. E., Caplan-Auerbach, J., Collins, J., et al. (2020). A Plan for a Long-Term, Automated,
 726 Broadband Seismic Monitoring Network on the Global Seafloor. *Seismological Research Letters*, 91(3), 1343–1355.
- 727 Kumar, M. R., & Bostock, M. G. (2008). Extraction of absolute P velocity from receiver functions. *Geophysical Journal International*, 175(2),
 728 515–519.
- 729 Kumar, P., Kawakatsu, H., Shinohara, M., Kanazawa, T., Araki, E., & Suyehiro, K. (2011). P and S receiver function analysis of seafloor
 730 borehole broadband seismic data. *Journal of Geophysical Research*, 116(B12), B12308.
- 731 Leahy, G. M., & Park, J. (2005). Hunting for oceanic island Moho. *Geophysical Journal International*, 160(3), 1020–1026.
- 732 Leahy, G. M., Collins, J. A., Wolfe, C. J., Laske, G., & Solomon, S. C. (2010). Underplating of the Hawaiian Swell: evidence from teleseismic
 733 receiver functions. *Geophysical Journal International*, 183(1), 313–329.
- 734 Lilly, J. M. (2017). jLab: A data analysis package for Matlab, v. 1.6. 5. See [Http://www.Jmlilly.Net/jmlsoft.Html](http://www.Jmlilly.Net/jmlsoft.Html).
- 735 Lin, P.-Y. P., Gaherty, J. B., Jin, G., Collins, J. A., Lizarralde, D., Evans, R. L., & Hirth, G. (2016). High-resolution seismic constraints on
 736 flow dynamics in the oceanic asthenosphere. *Nature*, 535(7613), 538–541.
- 737 Liu, Y., Liu, B., Liu, C., & Hua, Q. (2020). The crustal structure of the Eastern Subbasin of the South China Sea: constraints from receiver
 738 functions. *Geophysical Journal International*, 222(2), 1003–1012.
- 739 Lynner, C., JA Van Avendonk, H., Bécel, A., Christeson, G. L., Dugan, B., Gaherty, J. B., et al. (2020). The Eastern North American Margin
 740 Community Seismic Experiment: An Amphibious Active-and Passive-Source Dataset. *Seismological Research Letters*, 91(1), 533–540.
- 741 Mark, H. F., Lizarralde, D., & Collins, J. A. (2019). Azimuthal seismic anisotropy of 70-Ma Pacific-plate upper mantle. *Journal of*. Retrieved
 742 from <https://agupubs.onlinelibrary.wiley.com/doi/abs/10.1029/2018JB016451>
- 743 Ma, Z., Dalton, C. A., Russell, J. B., Gaherty, J. B., Hirth, G., & Forsyth, D. W. (2020). Shear attenuation and anelastic mechanisms in the
 744 central Pacific upper mantle. *Earth and Planetary Science Letters*, 536, 116148.
- 745 Olugboji, T. M., & Park, J. (2015). Crustal Anisotropy beneath selected Pacific-Ocean Islands from Harmonic Decomposition of Receiver
 746 Functions. In Revision, *Geochemistry Geophysics Geosystems*.
- 747 Olugboji, T. M., & Park, J. (2016). Crustal anisotropy beneath Pacific Ocean-Islands from harmonic decomposition of receiver functions.
 748 *Geochemistry, Geophysics, Geosystems*, 17(3), 810–832.
- 749 Olugboji, T. M., Karato, S.-I., & Park, J. (2013). Structures of the oceanic lithosphere–asthenosphere boundary: Mineral-physics modeling
 750 and seismological signatures. *Geochemistry, Geophysics, Geosystems*, 14(4), 880–901.
- 751 Olugboji, T. M., Park, J., Karato, S.-I., & Shinohara, M. (2016). Nature of the seismic lithosphere–asthenosphere boundary within normal
 752 oceanic mantle from high-resolution receiver functions. *Geochemistry, Geophysics, Geosystems*, 17(4), 1265–1282.
- 753 Olugboji, T. M., Park, J., & Karato, S.-I. (2016). Reply to comment by Kawakatsu and Abe on "Nature of the seismic
 754 lithosphere–asthenosphere boundary within normal oceanic mantle from high-resolution receiver functions." *Geochemistry, Geophysics,
 755 Geosystems*, 17(8), 3493–3501.
- 756 Osen, A., Amundsen, L., & Reitan, A. (1999). Removal of water-layer multiples from multicomponent sea-bottom data. *Geophysics*, 64(3),
 757 838–851.
- 758 Park, J., & Levin, V. (2000). Receiver Functions from Multiple-Taper Spectral Correlation Estimates. *Bulletin of the Seismological Society of
 759 America*, 90(6), 1507–1520.
- 760 Park, J., & Levin, V. (2016). Statistics and frequency-domain moveout for multiple-taper receiver functions. *Geophysical Journal International*,
 761 207(1), 512–527.
- 762 Park, J., & Rye, D. M. (2019). Why Is Crustal Underplating Beneath Many Hot Spot Islands Anisotropic? *Geochemistry, Geophysics, Geosystems*,
 763 20(11), 4779–4809.
- 764 Rondenay, S. (2009). Upper Mantle Imaging with Array Recordings of Converted and Scattered Teleseismic Waves. *Surveys in Geophysics*,
 765 30(4), 377–405.
- 766 Ruan, Y., Forsyth, D. W., & Bell, S. W. (2014). Marine sediment shear velocity structure from the ratio of displacement to pressure of
 767 Rayleigh waves at seafloor. *Journal of Geophysical Research, [Solid Earth]*, 119(8), 6357–6371.
- 768 Russell, J. B., Gaherty, J. B., Lin, P. P., Lizarralde, D., Collins, J. A., Hirth, G., & Evans, R. L. (2019). High-Resolution Constraints on Pacific
 769 Upper Mantle Petrofabric Inferred From Surface-Wave Anisotropy. *Journal of Geophysical Research, [Solid Earth]*, 124(1), 631–657.
- 770 Rychert, C., Harmon, N., Constable, S., & Wang, S. (2020). The nature of the Lithosphere–Asthenosphere Boundary. *Journal of Geophysical
 771 Research, [Solid Earth]*. <https://doi.org/10.1029/2018JB016463>
- 772 Rychert, C. a., Laske, G., Harmon, N., & Shearer, P. M. (2013). Seismic imaging of melt in a displaced Hawaiian plume. *Nature Geoscience*,
 773 6(8), 657–660.
- 774 Rychert, C. A., Harmon, N., & Tharimena, S. (2018a). Scattered wave imaging of the oceanic plate in Cascadia. *Science Advances*, 4(2),
 775 eaao1908.
- 776 Rychert, C. A., Harmon, N., & Tharimena, S. (2018b). Seismic Imaging of the base of the ocean plates. *Lithospheric Discontinuities*, 239, 71.
- 777 Sarafian, E., Evans, R. L., Collins, J. a., Elsenbeck, J., Gaetani, G. a., Gaherty, J. B., et al. (2015). The electrical structure of the central Pacific
 778 upper mantle constrained by the NoMelt experiment. *Geochemistry, Geophysics, Geosystems*, 16(4), 1115–1132.
- 779 Snieder, R., & Snieder, R. A. (2001). *A Guided Tour of Mathematical Methods: For the Physical Sciences*. Cambridge University Press.
- 780 Straume, E. O., Gaina, C., Medvedev, S., Hochmuth, K., Gohl, K., Whittaker, J. M., et al. (2019). GlobSed: Updated Total Sediment
 781 Thickness in the World's Oceans. *Geochemistry, Geophysics, Geosystems*, 20(4), 1756–1772.
- 782 Takeo, A., Kawakatsu, H., Isse, T., & Nishida, K. (2018). In Situ Characterization of the Lithosphere–Asthenosphere System beneath NW

- 783 Pacific Ocean Via Broadband Dispersion Survey With Two OBS Arrays. *Geochemistry: Exploration, Environment, Analysis*. Retrieved from
784 <https://agupubs.onlinelibrary.wiley.com/doi/abs/10.1029/2018GC007588>
- 785 Tan, Y., & Helmberger, D. V. (2007). Trans-Pacific upper mantle shear velocity structure. *Journal of Geophysical Research, [Solid Earth]*, 112(B8).
786 Retrieved from <https://agupubs.onlinelibrary.wiley.com/doi/abs/10.1029/2006JB004853>
- 787 Thorwart, M., & Dahm, T. (2005). Wavefield decomposition for passive ocean bottom seismological data. *Geophysical Journal International*,
788 163(2), 611–621.
- 789 Yeck, W. L., Sheehan, A. F., & Schulte-Pelkum, V. (2013). Sequential H- Stacking to Obtain Accurate Crustal Thicknesses beneath
790 Sedimentary Basins. *Bulletin of the Seismological Society of America*. <https://doi.org/10.1785/0120120290>
- 791 Yu, Y., Song, J., Liu, K. H., & Gao, S. S. (2015). Determining crustal structure beneath seismic stations overlying a low-velocity sedimentary
792 layer using receiver functions. *Journal of Geophysical Research, [Solid Earth]*, 120(5), 3208–3218.
- 793 Zhang, Z., & Olugboji, T. (2020). URseismology/RFDereverb: V1.0. <https://doi.org/10.5281/zenodo.4359598>
- 794 Zhu, L., & Kanamori, H. (2000). Moho depth variation in southern California from teleseismic receiver functions. *Journal of Geophysical
795 Research*, 105(B2), 2969–2980.